

Mask-Adapted Background Field Removal for Artifact Reduction in Quantitative Susceptibility Mapping of the Prostate

Sina Straub¹, Julian Emmerich¹, Heinz-Peter Schlemmer², Klaus H. Maier-Hein³, Mark E. Ladd¹, Matthias C. Röthke², David Bonekamp², and Frederik B. Laun^{1,4}

¹Department of Medical Physics in Radiology, German Cancer Research Center (DKFZ), Heidelberg, Germany; ²Department of Radiology, German Cancer Research Center (DKFZ), Heidelberg, Germany; ³Junior Group Medical Image Computing, German Cancer Research Center (DKFZ), Heidelberg, Germany; and ⁴Institute of Radiology, University Hospital Erlangen, Erlangen, Germany

Corresponding Author:

Sina Straub, PhD
Department of Medical Physics in Radiology,
German Cancer Research Center (DKFZ),
Im Neuenheimer Feld 280,
69120 Heidelberg, Germany;
E-mail: sina.straub@dkfz.de

Key Words: quantitative susceptibility mapping, prostate cancer, calcification, artifact reduction, background field removal

Abbreviations: Magnetic resonance imaging (MRI), quantitative susceptibility mapping (QSM), gradient-echo (GRE), magnetic resonance (MR), volumes of interest (VOIs)

ABSTRACT

We propose an alternative processing method for quantitative susceptibility mapping of the prostate that reduces artifacts and enables better visibility and quantification of calcifications and other lesions. Three-dimensional gradient-echo magnetic resonance data were obtained from 26 patients at 3 T who previously received a planning computed tomography of the prostate. Phase images were unwrapped using Laplacian-based phase unwrapping. The background field was removed with the V-SHARP method using tissue masks for the entire abdomen (Method 1) and masks that excluded bone and the rectum (Method 2). Susceptibility maps were calculated with the iLSQR method. The quality of susceptibility maps was assessed by one radiologist and two physicists who rated the data for visibility of lesions and data quality on a scale from 1 (poor) to 4 (good). The readers rated susceptibility maps computed with Method 2 to be, on average, better for visibility of lesions with a score of 2.9 ± 1.1 and image quality with a score of 2.8 ± 0.8 compared with maps computed with Method 1 ($2.4 \pm 1.2/2.3 \pm 1.0$). Regarding strong artifacts, these could be removed using adapted masks, and the susceptibility values seemed less biased by the artifacts. Thus, using an adapted mask for background field removal when calculating susceptibility maps of the prostate from phase data reduces artifacts and improves visibility of lesions.

INTRODUCTION

Prostate cancer is the most common cancer among males in the Western world (1). However, in magnetic resonance imaging (MRI), prostate cancer detection can be hampered by postbiopsy hemorrhage and/or calcifications (2); in particular, the detection of intraprostatic calcifications is difficult because of variations in signal intensity and the small size of the lesions (3). In addition, the treatment outcome may be influenced by the presence of calcifications (4, 5).

After quantitative susceptibility mapping (QSM) (6–8) had been successfully applied in several clinical studies of the brain (9–13), there have been in vivo applications of QSM in the liver (14, 15). Moreover, it has recently been shown that QSM can be a valuable tool to detect intra- and periprostatic calcifications (16), but in cases of intestinal movement or air in the rectum, severe artifacts can occur when inverting unreliable phase information because of nonlocality of the inversion kernel (17–21)

for QSM and can render the detection of calcifications difficult. Because streaking artifacts in susceptibility maps not only corrupt image quality and hamper detection of lesions (calcifications or hemorrhage), but also bias the accurate quantification of susceptibility values, the reduction or elimination of artifacts is crucial.

The purpose of this study is to propose a method to reduce or eliminate artifacts and enable better visibility of calcifications and other lesions, for example, hemorrhage, in the prostate.

METHODOLOGY

Patients

The study was conducted in accordance with the Declaration of Helsinki. Institutional review board approval was obtained, and all subjects provided written informed consent. Patient data were collected over the period of 1.3 years. In this study, 26 patients (age range: 55 to 80 years; mean age: 67.9 ± 6.8 years;

mean body mass index: 26.2 ± 3.5 kg/m²; range: 20.5 to 34.8 kg/m²) who had previously received planning computed tomography (CT) were included.

Data Acquisition

Magnitude and phase data used for QSM were acquired using a fully flow-compensated 3D gradient-echo (GRE) sequence that was part of a clinical protocol on two 3 T magnetic resonance (MR) scanners (Biograph mMR and MAGNETOM Prisma, Siemens Healthcare, Erlangen, Germany). The sequence was applied with the water excitation option switched on to suppress fat signals in 15 patients and was run without fat suppression in 12 patients. One patient was measured once with and once without fat suppression. Measurements on the Biograph mMR scanner were performed with an 8-channel surface coil; the acquisition parameters were as follows: flip angle = 15°, repetition time/echo time = 24/15 milliseconds, voxel size = $1.0 \times 1.0 \times 1.7$ mm³, acquisition matrix = $320 \times 240 \times 30$ –40, readout bandwidth = 822 Hz/pixel, and acquisition time = 5.55 minutes. Measurements on the MAGNETOM Prisma scanner were performed using an 18-channel surface coil with the following acquisition parameters: flip angle = 15°, repetition time/echo time = 24/20 milliseconds, voxel size = $0.83 \times 0.83 \times 1.6$ mm³, acquisition matrix = $384 \times 288 \times 36$, readout bandwidth = 765 Hz/pixel, phase and section partial Fourier = 7/8, and acquisition time = 4.52 minutes.

CT (Siemens and Philips scanners, Philips Healthcare, Hamburg, Germany) imaging parameters ranged from 120 to 140 kV peak, with slice thickness = 2–5 mm (3 mm for 20 patients), tube current–exposure time product = 93–300 mA · s (300 mA · s in 14 patients), and pitch factor = 0.6 to 1.5. A previous study has used the same data (16).

MR Data Processing

Phase images from different coils were combined on the scanner using the adaptive combine method (22). Phase images were unwrapped in Matlab (Matlab R2014b, The MathWorks, Inc., Natick, Massachusetts) using a Laplacian-based phase unwrapping algorithm (18, 23, 24). The background field was removed with sophisticated harmonic artifact reduction for phase data (V-SHARP) with varying spherical kernel sizes (up to 25 mm) (23, 24). First, masks encompassing the entire abdomen were used (“Method 1”). Second, masks encompassing the entire abdomen excluding bone and the rectum (if signal voids were present in the rectum) were used (“Method 2”). The masks were manually created using the Medical Imaging Interaction Toolkit (25, 26). Using the processed phase maps and the GRE magnitude data, susceptibility maps were calculated using the iLSQR method (18, 27). Susceptibility values were referenced (28) to the iliopsoas muscle (indicated in the first column in Figure 1 by “R”) as suggested by Straub et al. (16).

Data Analysis

Calcifications, both intraprostatic and phleboliths, were identified using CT data, and the volumes of interest (VOIs) encompassing them were drawn using the Medical Imaging Interaction Toolkit. In addition, VOIs for hemorrhages and a noncalcified control region in the prostate were drawn on GRE magnitude images/susceptibility maps. All mean susceptibility values and

standard deviations were calculated with Matlab as mean values over the specified VOIs after referencing the susceptibility values to the reference tissue.

In addition, the data were evaluated by three readers who were blinded to the CT data. Reader 1 was a radiologist with eight years of experience in assessing prostate MRI, whereas Readers 2 and 3 were physicists. They were provided with information about sections that contained lesions and were asked to rate the data for visibility of lesions and for image quality concerning the region of the prostate and the reference region (iliopsoas muscle) from 1 (poor) to 4 (good). They were asked to perform the following two rounds of scoring:

1. They were given the susceptibility maps i.e. calculated using Methods 1 and 2 of the 27 measurements. They were not provided with any information about the ordering. They were asked to consecutively rate the data.
2. They were asked to repeat the reading. For the second reading, the readers were provided with the susceptibility maps computed with Methods 1 and 2 in pairs. They were asked to compare these two paired maps and rate each of these maps according to the same criteria as in the first reading session.

RESULTS

Quality Assessment by Readers

When assessing all susceptibility maps separately, Reader 1 always rated the visibility of lesions as either equal or better for Method 2. The quality of the susceptibility maps in the region of the prostate and in the reference region was rated as either equal or better for Method 2 in 24 (out of 27) cases and in 20 (out of 27) cases, respectively, by Reader 1. Reader 2 rated the visibility of lesions and the quality of susceptibility maps in the region of the prostate/reference region always as either equal or better for Method 2 than for Method 1, except for one case, in which the visibility of lesions was rated better for Method 1. Reader 3 rated the visibility of lesions for Method 2 always as either equal or better with one exception. The quality of the susceptibility maps in the region of the prostate and in the reference region was rated as either equal or better in 24 (out of 27) cases by Reader 3.

When directly comparing the susceptibility maps computed by Methods 1 and 2, the readers always rated the susceptibility maps as either equal or better for Method 2. The mean scores of the three readers are shown in Table 1.

Image Data

Figure 1 shows susceptibility maps of four patients computed with a mask including the entire abdomen (Method 1) and a mask where bones and rectum were excluded (Method 2). In addition, the difference of the susceptibility maps calculated using Method 1 and Method 2 is shown as well as the unwrapped phase map. In Patients 2 and 13, strong artifacts (thick arrows) can be observed close to the rectum when using Method 1. These artifacts coincide with large field distortions seen on the phase maps. In Patients 2 and 13, these artifacts lie exactly in the region where the calcifications are located (white arrow heads). In these cases, susceptibility values differ more strongly between the two

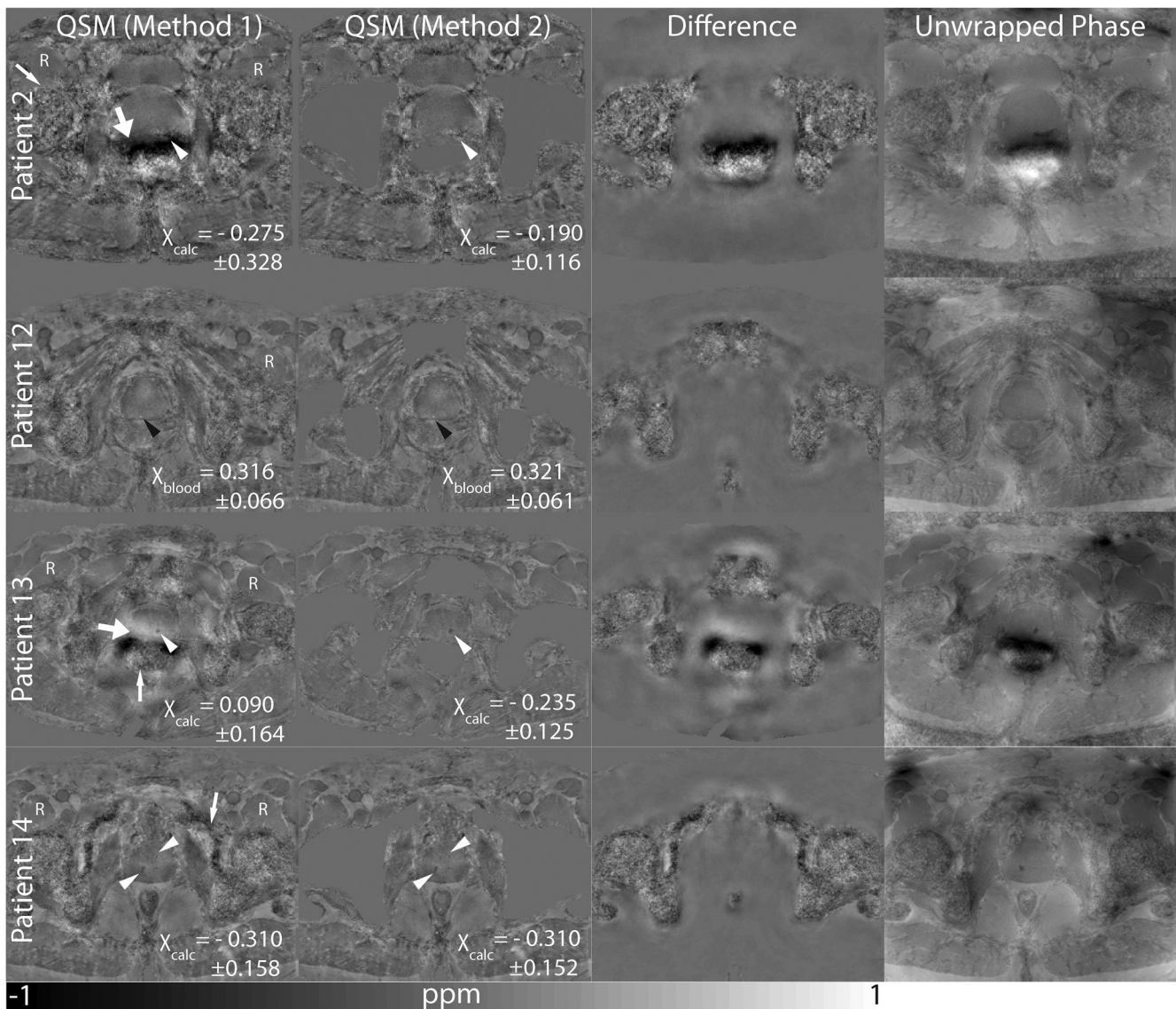


Figure 1. Susceptibility maps (Method 1) and susceptibility maps calculated using an adapted mask (Method 2). The difference of the susceptibility maps calculated using both methods is shown as well as the unwrapped phase. Calcifications are indicated by white arrow heads, and bleeding is indicated by black arrow heads. Motion/air artifacts (thick white arrows) and noise (thin white arrows) can be observed. The reference region is indicated by the letter “R”.

methods than for the two susceptibility maps without strong artifacts (Patients 12, 14). Using Method 1 results in more regions in which strong noise can be observed (thin arrows), which, however, does not strongly affect the visibility of the prostate itself or the reference region.

Susceptibility Values

Figure 2 shows mean susceptibility values with standard deviations of all measurements for calcifications in the prostate, phleboliths, hemorrhage, a noncalcified control region in the prostate, and the reference region (iliopsoas muscle). Mean susceptibility values differ only slightly between the two methods, but standard deviations are lower for Method 2.

DISCUSSION

In particular, in cases where severe artifacts from intestinal movements or air tissue interfaces impair the quality of susceptibility maps, masking such regions and therefore treating the field distortions they cause as artificial background field may be a viable option to reliably obtain clinically useful susceptibility maps that allow good depiction and quantification of calcifications or hemorrhage.

A similar approach to increase susceptibility maps' quality by masking out problematic regions has been proposed to reduce artifacts when calculating susceptibility maps of the brain when hemorrhage is present (29): the hemorrhage is masked by thresholding, and susceptibility maps are calculated both for the

Table 1. Quality Assessment by the Readers

Assessment of Susceptibility Maps by the three Readers	Method 1			Method 2		
	Reader 1	Reader 2	Reader 3	Reader 1	Reader 2	Reader 3
Visibility of the Lesions	2.7 ± 1.4	2.1 ± 0.9	2.5 ± 1.3	3.3 ± 1.1	2.4 ± 1.1	3.0 ± 1.1
	2.4 ± 1.2			2.9 ± 1.1		
Quality of the Susceptibility Map in the Prostate Region	2.5 ± 0.9	1.9 ± 0.9	2.5 ± 0.9	2.9 ± 0.8	2.4 ± 0.7	3.3 ± 0.7
	2.3 ± 1.0			2.8 ± 0.8		
Quality of the Susceptibility Map in the Reference Region	2.7 ± 0.8	2.1 ± 0.7	3.7 ± 0.4	2.6 ± 0.6	2.1 ± 0.7	3.7 ± 0.5
	2.9 ± 0.9			2.8 ± 0.9		
Visibility of the Lesions (Direct Comparison)	3.1 ± 1.2	2.1 ± 0.8	2.9 ± 1.2	3.3 ± 1.2	2.5 ± 1.0	3.1 ± 1.1
	2.7 ± 1.1			2.9 ± 1.1		
Quality of the Susceptibility Map in the Prostate Region (Direct Comparison)	2.2 ± 0.8	1.9 ± 0.8	2.7 ± 0.9	3.1 ± 0.8	2.6 ± 0.8	3.0 ± 0.8
	2.3 ± 0.9			2.9 ± 0.8		
Quality of the Susceptibility Map in the Reference Region (Direct Comparison)	2.6 ± 0.6	2.4 ± 0.6	3.8 ± 0.6	3.2 ± 0.7	2.7 ± 0.6	3.8 ± 0.6
	2.9 ± 0.9			3.2 ± 0.8		

Note: Scores ranged from 1 (poor) to 4 (good). Mean and standard deviation of scores for each reader individually and of scores for all readers are shown.

mask of the whole brain and the mask excluding the hemorrhage. These two susceptibility maps are then superposed to obtain a susceptibility map where artifacts are either reduced or eliminated. In the case of the prostate, it has to be evaluated whether mask generation can be performed automatically, for example, using active appearance models, atlas registration, or level sets (30) on GRE magnitude data, as prostate MRI image segmentation has been an area of intense research because of the increased use of MRI as a modality for the clinical workup of prostate cancer. Similar approaches may be applicable to investigations of other organs in which air tissue interfaces or motion are inevitably present during imaging. In contrast, in the case of motion, triggering, or motility-reducing medication (i.e., hyoscine butylbromide) may be further options to reduce artifacts.

The assessment of prostatic calcifications with MRI techniques can be of importance in various applications, such as in radiation therapy and high intensity focused ultrasound pro-

static calcifications can influence dose and therefore treatment outcome (4, 5); and calcifications can be used as a position marker in image-guided therapy (3). Moreover, knowledge about calcifications may gain importance in future applications, for example, MR-linac procedures (31).

Limitations of this study include the small number of patients and the use of different scanners with slightly different imaging parameters. Moreover, drawing masks of the abdomen in which bones and the rectum are excluded can be very time-consuming. In addition, the effect of using a multiecho acquisition and water-fat separation (32, 33) on the quality of susceptibility maps of the prostate has to be assessed in the future.

In conclusion, using adapted masks for susceptibility map calculation can efficiently eliminate severe artifacts and enable correct quantification of susceptibility in the prostate even in difficult cases of intestinal movement or air in the rectum.

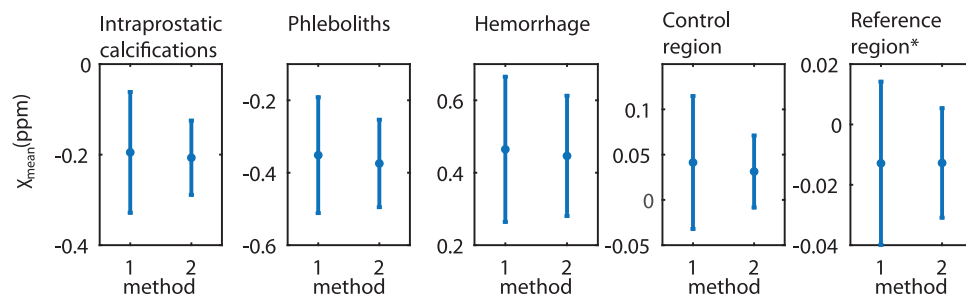


Figure 2. Mean susceptibility values in all patients for calcifications (first column), phleboliths (second column), hemorrhage (third column), control region (fourth column), and reference region (fifths column). Method 1: the mask included the entire abdomen. Method 2: rectum and bones were excluded. *All susceptibility values are referenced to the iliopsoas muscle except for the reference region itself, which is not referenced to a specific reference region.

REFERENCES

1. Ferlay J, Soerjomataram I, Ervik M, Dikshit R, Eser S, Mathers C, Rebelo M, Parkin DM, Forman D, Bray, F. GLOBOCAN 2012 v1.0. Cancer Incidence and Mortality Worldwide: IARC CancerBase No. 11. Lyon, France: International Agency for Research on Cancer; 2013. <http://globocan.iarc.fr>.
2. Barentsz JO, Richenberg J, Clements R, Choyke P, Verma S, Villeirs G, Rouviere O, Logager V, Fütterer JJ; European Society of Urogenital Radiology. ESUR prostate MR guidelines 2012. *Eur Radiol.* 2012;22(4):746–757.
3. Zeng GG, McGowan TS, Larsen TM, Bruce LM, Moran NK, Tsao JR, MacPherson MS. Calcifications are potential surrogates for prostate localization in image-guided radiotherapy. *Int J Radiat Oncol Biol Phys.* 2008;72(4):963–966.
4. Pope DJ, Cutajar DL, George SP, Guatelli S, Bucci JA, Enari KE, Miller S, Siegle R, Rosenfeld AB. The investigation of prostatic calcifications using μ -PIXE analysis and their dosimetric effect in low dose rate brachytherapy treatments using Geant4. *Phys Med Biol.* 2015;60(11):4335–4353.
5. Mason J, Al-Qaisieh B, Bownes P, Henry A, Thwaites D. Investigation of interseed attenuation and tissue composition effects in ^{125}I seed implant prostate brachytherapy. *Brachytherapy.* 2014;13(6):603–610.
6. Haacke EM, Liu S, Buch S, Zheng W, Wu D, Ye Y. Quantitative susceptibility mapping: current status and future directions. *Magn Reson Imaging.* 2015;33(1):1–25.
7. Wang Y, Liu T. Quantitative susceptibility mapping (QSM): Decoding MRI data for a tissue magnetic biomarker. *Magn Reson Med.* 2015;73(1):82–101.
8. Schweser F, Deistung A, Reichenbach JR. Foundations of MRI phase imaging and processing for Quantitative Susceptibility Mapping (QSM). *Z Med Phys.* 2016;26(1):6–34.
9. Chen W, Gauthier SA, Gupta A, Comunale J, Liu T, Wang S, Pei M, Pitt D, Wang Y. Quantitative susceptibility mapping of multiple sclerosis lesions at various ages. *Radiology.* 2014;271(1):183–192.
10. Langkammer C, Liu T, Khalil M, Enzinger C, Jehna M, Fuchs S, Fazekas F, Wang Y, Ropele S. Quantitative susceptibility mapping in multiple sclerosis. *Radiology.* 2014;267(2):551–559.
11. Liu T, Eskreis-Winkler S, Schweitzer AD, Chen W, Kaplitt MG, Tsiouris AJ, Wang Y. Improved subthalamic nucleus depiction with quantitative susceptibility mapping. *Radiology.* 2013;269(1):216–223.
12. Al-Radaideh AM, Wharton SJ, Lim SY, Tench CR, Morgan PS, Bowtell RW, Constantinescu CS, Gowland PA. Increased iron accumulation occurs in the earliest stages of demyelinating disease: an ultra-high field susceptibility mapping study in clinically isolated syndrome. *Mult Scler.* 2013;19(7):896–903.
13. Loffipour AK, Wharton S, Schwarz ST, Gontu V, Schäfer A, Peters AM, Bowtell RW, Auer DP, Gowland PA, Bajaj NP. High resolution magnetic susceptibility mapping of the substantia nigra in Parkinson's disease. *J Magn Reson Imaging.* 2012;35(1):48–55.
14. Hernando D, Cook RJ, Diamond C, Reeder SB. Magnetic susceptibility as a B0 field strength independent MRI biomarker of liver iron overload. *Magn Reson Med.* 2013;70(3):648–656.
15. Sharma SD, Hernando D, Horng DE, Reeder SB. Quantitative susceptibility mapping in the abdomen as an imaging biomarker of hepatic iron overload. *Magn Reson Med.* 2015;74(3):673–683.
16. Straub S, Laun FB, Emmerich J, Jobke B, Hauswald H, Katayama S, Herfarth K, Schlemmer HP, Ladd ME1, Ziener CH, Bonekamp D, Röthke MC. Potential of quantitative susceptibility mapping for detection of prostatic calcifications. *J Magn Reson Imaging.* 2016;45(3):889–898.
17. Shmueli K, de Zwart JA, van Gelderen P, Li TQ, Dodd SJ, Duyn JH. Magnetic susceptibility mapping of brain tissue in vivo using MRI phase data. *Magn Reson Med.* 2009;62(6):1510–1522.
18. Li W, Wu B, Liu C. Quantitative susceptibility mapping of human brain reflects spatial variation in tissue composition. *Neuroimage.* 2011;55(4):1645–1656.
19. Liu T, Wisniewski C, Lou M, Chen W, Spincemaille P, Wang Y. Nonlinear formulation of the magnetic field to source relationship for robust quantitative susceptibility mapping. *Magn Reson Med.* 2013;69(2):467–476.
20. De Rochefort L, Brown R, Prince MR, Wang Y. Quantitative MR susceptibility mapping using piece-wise constant regularized inversion of the magnetic field. *Magn Reson Med.* 2008;60(4):1003–1009.
21. Wen Y, Wang Y, Liu T. Enhancing k-space quantitative susceptibility mapping by enforcing consistency on the cone data (CCD) with structural priors. *Magn Reson Med.* 2016;75(2):823–830.
22. Prock T, Collins DJ, Dzik-Jurasz ASK, Leach MO. An algorithm for the optimum combination of data from arbitrary magnetic resonance phased array probes. *Phys Med Biol.* 2002;47(2):N39–N46.
23. Li W, Avram AV, Wu B, Xiao X, Liu C. Integrated Laplacian-based phase unwrapping and background phase removal for quantitative susceptibility mapping. *NMR Biomed.* 2014;27(2):219–227.
24. Wu B, Li W, Guidon A, Liu C. Whole brain susceptibility mapping using compressed sensing. *Magn Reson Med.* 2012;67(1):137–147.
25. Maleike D, Nolden M, Meinzer HP, Wolf I. Interactive segmentation framework of the Medical Imaging Interaction Toolkit. *Comput Methods Programs Biomed.* 2009;96(1):72–83.
26. Nolden M, Zelzer S, Seitel A, Wald D, Müller M, Franz AM, Maleike D, Fangerau M, Baumhauer M, Maier-Hein L, Maier-Hein KH, Meinzer HP, Wolf I. The Medical Imaging Interaction Toolkit: challenges and advances: 10 years of open-source development. *Int J Comput Assist Radiol Surg.* 2013;8(4):607–620.
27. Li W, Wang N, Yu F, Han H, Cao W, Romero R, Tantiwongkosi B, Duong TQ, Liu C. A method for estimating and removing streaking artifacts in quantitative susceptibility mapping. *Neuroimage.* 2015;108:111–122.
28. Straub S, Schneider T, Emmerich J, Freitag MT, Ziener CH, Schlemmer HP, Ladd ME, Laun FB. Suitable reference tissues for quantitative susceptibility mapping of the brain. *Magn Reson Med.* 2016. [Epub ahead of print].
29. Sun H, Kate M, Gioia LC, Emery DJ, Butcher K, Wilman AH. Quantitative susceptibility mapping using a superposed dipole inversion method: application to intracranial hemorrhage. *Magn Reson Med.* 2015;76(3):781–791.
30. Litjens G, Toth R, van de Ven W, Hoeks C, Kerkstra S, van Ginneken B, Vincent G, Guillard G, Birbeck N, Zhang J, Strand R, Malmberg F, Ou Y, Davatzikos C, Kirschner M, Jung F, Yuan J, Qiu W, Gao Q, Edwards PE, Maan B, van der Heijden F, Ghose S, Mitra J, Dowling J, Barratt D, Huisman H, Madabhushi A. Evaluation of prostate segmentation algorithms for MRI: the PROMISE12 challenge. *Med Image Anal.* 2014;18(2):359–373.
31. Prior P, Chen X, Botros M, Paulson ES, Lawton C, Erickson B, Li XA. MRI-based IMRT planning for MR-linac: comparison between CT- and MRI-based plans for pancreatic and prostate cancers. *Phys Med Biol.* 2016;61(10):3819–3842.
32. Dimov AV, Liu T, Spincemaille P, Ecanow JS, Tan H, Edelman RR, Wang Y. Joint estimation of chemical shift and quantitative susceptibility mapping (chemical QSM). *Magn Reson Med.* 2015;73(6):2100–2110.
33. Sharma SD, Hernando D, Horng DE, Reeder SB. Quantitative susceptibility mapping in the abdomen as an imaging biomarker of hepatic iron overload. *Magn Reson Med.* 2015;74(3):673–683.